Journal of Computational Physics **154,** 342–371 (1999)
Article ID jcph.1999.6316, available online at http://www.idealibrary.com on IDEAL®

A Consistent Hybrid Finite-Volume/Particle Method for the PDF Equations of Turbulent Reactive Flows

Metin Muradoglu, Patrick Jenny, Stephen B. Pope, and David A. Caughey

Sibley School of Mechanical and Aerospace Engineering, Cornell University, Ithaca, New York 14853
E-mail: {metinm, jenny, pope, caughey}@mae.cornell.edu

Received December 1, 1998; revised May 19, 1999

The paper describes a new hybrid finite-volume (FV)/particle method developed for the solution of the PDF equations for statistically stationary turbulent reactive flows. In this approach, the conservation equations for mean mass, momentum, and energy conservation are solved by a FV method while a particle algorithm is employed to solve the fluctuating velocity-turbulence frequency-compositions joint PDF transport equation. The mean velocity and pressure are supplied to the particle code by the FV code which in turn obtains all the Reynolds stresses, the scalar fluxes, and the reaction terms needed in the FV code. An important feature of the method is the complete consistency between the set of equations solved by the FV and particle methods. The algorithmic and numerical issues arising in the development of the hybrid method are studied in the simple setting of the stochastic ideal flow equations. Numerical results are obtained for 1D reactive stochastic ideal flow to demonstrate numerical properties of the method. The total numerical error is identified as statistical error, bias, spatial truncation error, and temporal truncation error. In contrast to the self-contained particle method, the bias is found to be negligibly small. It is shown that all the numerical errors converge at the expected rates. Finally, the global convergence of the hybrid method is demonstrated and the optimal strategy for time-averaging that gives the best global convergence rate is investigated.

Key Words: hybrid finite-volume/particle method; numerical convergence; reactive stochastic ideal flows.

1. INTRODUCTION

The probability density function (PDF) method has proven to be a useful computational tool for analysis of complex turbulent reacting flows [1]. Compared to traditional moment-closure methods, the PDF method offers the distinct advantages of being able to treat convection and finite-rate nonlinear chemistry exactly [2, 3]. In addition to this, body forces

0021-9991/99 $30.00

and the mean pressure gradient also appear in closed form, but the fluctuating pressure gradient and molecular transport terms need to be modeled [2].

In PDF methods, a modeled evolution equation is solved for the one-point joint PDF of the selected flow variables. The PDF transport equation is derived from the Navier–Stokes equations and the unclosed terms are modeled by coupled model stochastic differential equations (SDEs) [3]. Due to the high dimensionality of the PDF, conventional numerical techniques such as finite-difference and finite-element methods are computationally prohibitive. However, efficient solutions to the modeled joint PDF transport equation are made feasible by use of a particle-mesh Monte Carlo method in which the PDF is represented by a large set of stochastic particles [2]. We note that the PDF equations can be alternatively solved by a purely particle Monte Carlo method through use of smoothed particle hydrodynamics (SPH) where no field equations are solved and neither is a mesh needed to extract statistical means [5]. The PDF equations can be modeled and solved by either an Eulerian or a Lagrangian method. In the Eulerian method [4] the particles are located at grid nodes in physical space while in the Lagrangian method the particles are continuously distributed. The Lagrangian viewpoint has been central to the PDF methods for over a decade, since it makes modeling simpler and offers an intuitively obvious solution algorithm [1, 3]. The particle properties evolve according to model stochastic differential equations (SDEs), and there are usually one or more mean fields that are determined separately by solution of partial differential equations (PDEs) on a mesh. Various mean fields can also be estimated from the particles and we refer to these as "particle fields" to distinguish them from the "mean fields" obtained from PDEs. The mean and particle fields and their use in the particle equations make an important distinction between different PDF solution algorithms. Table I summarizes attributes of different Lagrangian solution algorithms some of which are discussed further in the following section.

1.1. *Review of PDF Algorithms*

In some early applications of PDF methods, a finite volume (FV) method is coupled with a particle method based on the joint PDF of compositions (or of velocity and compositions) to provide additional turbulence closure equations. Such a hybrid algorithm has been proposed by Anand *et al.* [21] and Haworth and El Tahry [22] in which the modeled transport equation for the joint PDF of velocity and composition is solved by the Monte Carlo method, while a SIMPLE [6] based FV algorithm is employed to solve the Reynolds-averaged flow equations. In this approach, the FV code provides the Monte Carlo code with the mean velocity, pressure, and rate of turbulence dissipation, and the Monte Carlo code in turn supplies the Reynolds stresses and mean density to the FV code. The mean velocity appears to be a duplicate field, i.e., it is represented both as a particle field and as a mean field.

A similar hybrid method has also been developed by Correa and Pope [14] and implemented in the code *PDF2DS*. This method makes minimal use of particle properties, i.e., the mean velocity, pressure, turbulence kinetic energy, and rate of dissipation needed in the particle equations are supplied by the FV method which in turn gets the mean particle density field from the Monte Carlo code. The duplicate fields include the mean velocity and Reynolds stresses. The same algorithm has also been used by Chang [15], Tsai and Fox [16], Wouters *et al.* [18], and Nau *et al.* [19].

As mentioned above, some fields are represented as duplicate fields, which raises questions of consistency. In these hybrid methods, the consistency conditions are not fully

TABLE I
Attributes of Different Lagrangian PDF Solution Algorithms[a]

Method	Particle equations			Mean field equations		
	Particle properties	Particle fields used in particle equations	Mean fields used in particle equations	Mean field variables	Particle fields used in mean field equations	Duplicate fields
Composition jpdf (Pope [2])	$m^*, \mathbf{Y}^*$	$\tilde{\mathbf{Y}}, \overline{\rho}$	$\tilde{\mathbf{U}}, k, \epsilon$	$\tilde{\mathbf{U}}, \langle p\rangle, k, \epsilon$	$\overline{\rho}$	—
Composition jpdf (Jaberi *et al.* [20])	$m^*, \mathbf{Y}^*, z(\mathbf{Y}^*)$	$\tilde{\mathbf{Y}}$	$\tilde{\mathbf{U}}, \overline{\rho}, k, \epsilon$	$\tilde{\mathbf{U}}, \langle p\rangle, \tilde{z}$ $\overline{\rho}, k, \epsilon$	$\tilde{\tilde{z}}, \langle u_i^* z^* \mid \mathbf{x}\rangle$	$\tilde{z}$
Velocity-composition jpdf, minimal use of particle properties (*PDF2DS* [14])	$m^*, \mathbf{U}^*, \mathbf{Y}^*$	$\tilde{\mathbf{Y}}, \overline{\rho}$	$\tilde{\mathbf{U}}, k, \epsilon$ $\langle p\rangle$	$\tilde{\mathbf{U}}, \langle p\rangle, k, \epsilon$	$\overline{\rho}$	$\tilde{\mathbf{U}}, \langle u_i u_j\rangle$
Velocity-composition jpdf, maximal use of particle properties (Anand *et al.* [21] Haworth and El Tahry [22])	$m^*, \mathbf{U}^*, \mathbf{Y}^*$	$\tilde{\mathbf{Y}}, k$	$\tilde{\mathbf{U}}, \epsilon, \langle p\rangle$	$\tilde{\mathbf{U}}, \langle p\rangle, \epsilon$	$\overline{\rho}, \langle u_i^* u_j^* \mid \mathbf{x}\rangle$	$\tilde{\mathbf{U}}$
Velocity-frequency-composition jpdf (*PDF2DV* [9])	$m^*, \mathbf{U}^*, \omega^*, \mathbf{Y}^*$	$\tilde{\mathbf{U}}, \tilde{\mathbf{Y}}, \overline{\rho}, \tilde{\omega}, \Omega,$ $\langle u_i^* u_j^* \mid \mathbf{x}\rangle$	$\langle p\rangle$	$\langle p\rangle$	$\langle \rho^* \mathbf{U}^* \mid \mathbf{x}\rangle$	—
Velocity-frequency-composition jpdf SPH (Welton and Pope [5])	$m^*, \mathbf{U}^*, \omega^*,$ $\mathbf{Y}^*, p^*$	$\tilde{\mathbf{U}}, \tilde{\mathbf{Y}}, \tilde{\omega}, \langle p\rangle,$ $\langle u_i^* u_j^* \mid \mathbf{x}\rangle$	—	—	—	—
Velocity-frequency-composition jpdf (present)	$m^*, \mathbf{u}^*, \omega^*,$ $\mathbf{Y}^*, h^*$	$\tilde{\mathbf{Y}}, \overline{\rho}, \tilde{\omega}, \Omega,$ $\langle u_i^* u_j^* \mid \mathbf{x}\rangle$	$\tilde{\mathbf{U}}, \langle p\rangle$	$\tilde{\mathbf{U}}, \langle p\rangle, \tilde{\epsilon}_s, \overline{\rho}$	$\langle u_i^* u_j^* \mid \mathbf{x}\rangle, \tilde{\tilde{\epsilon}}_s$ $\langle u_i^* \epsilon_s^* \mid \mathbf{x}\rangle$	$\overline{\rho}, \tilde{\epsilon}_s$

[a] $k, \epsilon, z, \tilde{\tilde{z}}, \langle u_i^* z^* \mid \mathbf{x}\rangle, \omega$, and Ω are the mean turbulent kinetic energy, the mean dissipation rate, an energy variable, the mean rate of change in the energy variable, i.e., $\tilde{\tilde{z}} = d\tilde{z}/dt$, the scalar fluxes, the instantaneous turbulent frequency, and the conditional mean turbulent frequency, respectively. The definition of means, e.g., $\tilde{\omega}$, and the other variables are the same as defined in the paper.

satisfied even at the level of turbulence closures due to the inconsistency of the turbulence models employed in FV and PDF submodels. For example, the simplified Langevin model (SLM) is equivalent to the Rotta model at the level of second moments [17]. Thus, use of a $k-\epsilon$ model in the FV code and of a SLM PDF model in the particle code cannot be consistent. As shown by Wouters *et al.* [18], the level of consistency mainly depends on the equivalence of the turbulence models used in FV and PDF methods.

In addition to the consistency problem, it has been found that the use of a noisy particle density field in the mean field equations causes a serious convergence problem that can hinder and even prevent convergence of the FV method (see, e.g., Chang [15]). An alternative method developed by Jaberi *et al.* [20] is designed to overcome the difficulty caused by the noise in the particle density field. In this method, in addition to other quantities, mean field

equations are solved for the mean density and mean energy variable. The mean pressure is then obtained from the mean equation of state. The resulting noise in the mean density field is substantially reduced compared to that of the particle density field.

With the relatively recent development of a model for turbulence frequency (or time scale), the velocity-frequency-composition joint PDF method forms a complete turbulence model which requires no further information except for fluid properties and initial and boundary conditions [7, 8]. Therefore, this model allows development of a consistent self-contained particle method. Such a self-contained particle-mesh based Monte Carlo algorithm has been developed and implemented in the *PDF2DV* code in which, except for mean pressure field, the particle fields are used throughout in the particle equations [9]. While *PDF2DV* successfully solves the modeled velocity-frequency-compositions joint PDF transport equation, two important shortcomings have been identified [10, 12]:

(i) a complicated algorithm is required for calculation of the mean pressure field, that needs damping and dissipation, and may not be very accurate on the grids typically used [11];

(ii) the use of the particle mean velocity in the particle equations has been found to lead to substantial deterministic error called bias [12].

It is emphasized here that all the shortcomings listed above are related to experience with the versions of the *PDF2DV* code which represent only a particular implementation of self-contained particle/mesh method. However, there has been reported no other implementation of a self-contained particle/mesh algorithm which has been extensively tested.

1.2. *Present Method*

These deficiencies in the self-contained particle method motivate the development of a new hybrid algorithm which combines the best features of FV and particle methods to avoid the shortcomings just mentioned. In this approach, the conservation equations for mean mass, momentum, and energy, coupled with a mean equation of state are solved by a FV method while a particle-mesh based Monte Carlo algorithm is employed to solve the modeled transport equation of joint PDF for fluctuating velocity, turbulence frequency, enthalpy, and compositions. The FV and particle codes are linked as follows. The FV code provides the particle code with the mean velocity and pressure while the particle code supplies all the turbulence quantities and the chemical source terms needed in the FV code. Therefore, the bias error is substantially reduced by the use of the smooth mean velocity field and the need for additional turbulence and chemistry models in the FV method is avoided. Furthermore, the mean pressure is easily computed from the mean equation of state. In this method, the mean density and mean sensible internal energy are duplicate fields. It is emphasized that this hybrid algorithm is completely consistent at the level of turbulence closure so that the consistency conditions are easily satisfied.

The purpose of this work is to address the algorithmic and numerical issues associated with the present hybrid FV/particle method such as coupling, convergence, and statistical and deterministic errors which have not been examined extensively in any of the previous studies on hybrid methods.

The approach taken here is to study all these issues in the simpler setting of reactive stochastic ideal flow. This is a non-physical system in which, from random initial conditions, flow properties evolve deterministically according to the ideal flow equations. It is especially valuable that for this class of flows there is an exact correspondence between particle and

field equations. In addition to this, even 1D stochastic ideal flows have the ingredients needed to address the issues arising in the context of developing a hybrid FV/particle algorithm for tubulent reacting flows. Therefore, the analysis is done in the simple one-dimensional setting that makes it possible to consider extreme cases such as very large numbers of particles per cell and time-averaging over long time periods.

1.3. *Outline of the Paper*

The paper starts with a brief description of the governing equations of reactive stochastic ideal flow: The thermochemistry is reviewed and the systems of equations solved by the particle and FV methods are presented. The mean fields used in the particle system and the particle fields used in the FV system are shown and the consistency conditions are identified. The numerical methods are discussed in Section 3. The FV and particle schemes are described in the context of the hybrid FV/particle algorithm. Numerical results are presented and discussed in Section 4. Some sample flow calculations are shown and a detailed analysis of the numerical errors arising in the hybrid method is presented. A comprehensive convergence study is also presented in this section. The results clearly demonstrate consistency, stability, convergence, accuracy, and efficiency of the hybrid method. Conclusions are drawn in Section 5. Finally, the derivation of the reactive stochastic ideal flow equations is provided separately in the Appendix.

2. GOVERNING EQUATIONS

A number of numerical and algorithmic issues arising in the development of a hybrid FV/particle method for turbulent reactive flows can be studied in the simpler system of the stochastic ideal flow of a reactive gas mixture. The purpose of this section is briefly to review the thermochemistry involved and to describe the evolution equations to be solved by the particle and FV methods. The derivation of the equations is supplied in the Appendix.

2.1. *Thermochemistry*

The thermochemical state of a homogeneous mixture of ideal gases is characterized by the pressure p, the temperature T, and the mass fractions of the N_s species $\mathbf{Y} = \{Y_1, Y_2, \ldots, Y_{N_s}\}$. As described in the Appendix, for each species ($\alpha = 1, 2, \ldots, N_s$), the following properties are defined: the gas constant R_α, the specific enthalpy $h_\alpha(T)$, and the specific sensible internal energy $\epsilon_{s_\alpha}(T)$. The corresponding mixture properties (i.e., $R(\mathbf{Y}, T)$, $h(\mathbf{Y}, T)$, and $\epsilon_s(\mathbf{Y}, T)$) are defined by, for example,

$$h(\mathbf{Y}, T) \equiv \sum_\alpha Y_\alpha h_\alpha(T). \tag{1}$$

The ideal gas law is

$$p = \rho R T, \tag{2}$$

where ρ is the density. This can also be written as

$$p = \rho \kappa \epsilon_s, \tag{3}$$

where κ is defined by

$$\kappa(\mathbf{Y}, T) = \frac{RT}{\epsilon_s}. \tag{4}$$

Note that if R and c_v are constant then κ is the constant $R/c_v = \gamma - 1$ where γ is the ratio of specific heats. In general, κ can be expected to depend weakly on $\mathbf{Y}$ and T.

The net chemical reaction rate for species α is S_α, so that, for a homogeneous mixture, the mass fractions evolve by

$$\frac{dY_\alpha}{dt} = S_\alpha(\mathbf{Y}, p, T). \tag{5}$$

2.2. *Stochastic Ideal Flow*

As an intermediate step between ideal and turbulent flows, we consider here a non-physical system, in which—from random initial and inflow boundary conditions—the flow properties evolve deterministically according to the ideal flow equations. The governing equations are described here in the context of the hybrid FV/particle method.

2.2.1. Particle system. The flow equations written in the convective form describe the evolution of the properties of the fluid particles. The particle system is described here for a closed system, i.e., one in which there is no mass flow in or out. The results are the same for an open system but the analysis is more complicated. The intrinsic properties of a general particle include mass m^*, position $\mathbf{X}^*(t)$, fluctuating velocity $\mathbf{u}^*(t)$, mass fractions $\mathbf{Y}^*(t)$, and enthalpy $h^*(t)$. It is emphasized that these properties are random and that there are no underlying random fields. There are, however, non-random pressure $p(\mathbf{x}, t)$ and mean velocity $\tilde{\mathbf{U}}(\mathbf{x}, t)$ fields. The thermochemical state of the particles is completely determined by $\mathbf{Y}^*(t)$, $h^*(t)$, and the interpolated pressure $p^*(t)$. Note that, here and below, an asterisk on a field variable (e.g., p^*) denotes the value of the field evaluated at the particle location, i.e.,

$$p^*(t) \equiv p(\mathbf{X}^*[t], t). \tag{6}$$

The intrinsic properties (m^*, $\mathbf{X}^*$, $\mathbf{u}^*$, $\mathbf{Y}^*$, and h^*), the interpolated mean velocity $\tilde{\mathbf{U}}^*$ and mean pressure p^* are called the primary properties. These properties contain no redundancy: no one of them can be deduced from the others. Nevertheless, various secondary particle properties can be derived from the primary properties such as density ρ^*, specific volume $v^* \equiv 1/\rho^*$, temperature T^*, and sensible internal energy ϵ_s^*.

From the particle properties, various particle fields can be estimated. The *expected particle mass density* $\bar{\rho}(\mathbf{x}, t)$ is defined by

$$\bar{\rho}(\mathbf{x}, t) = q(\mathbf{x}, t) \equiv \langle m^* \delta(\mathbf{X}^*[t] - \mathbf{x}) \rangle. \tag{7}$$

For a particle property ϕ^*, the *mass-weighted conditional expectation* is defined by

$$\begin{aligned} \tilde{\phi}(\mathbf{x}, t) &\equiv \langle \phi^*(t) \mid \mathbf{X}^*(t) = \mathbf{x} \rangle \\ &= \langle m^* \phi^*(t) \delta(\mathbf{X}^*[t] - \mathbf{x}) \rangle / \bar{\rho}(\mathbf{x}, t). \end{aligned} \tag{8}$$

Note that for $\phi \equiv 1$, $\tilde{\phi}$ is unity. The *volume-weighted conditional expectation* is defined by

$$\begin{aligned}\bar{\phi}(\mathbf{x}, t) &\equiv \langle \phi^*(t) v^*(t) \mid \mathbf{X}^*(t) = \mathbf{x} \rangle \bar{\rho}(\mathbf{x}, t) \\ &= \langle m^* \phi^*(t) v^*(t) \delta(\mathbf{X}^*[t] - \mathbf{x}) \rangle. \end{aligned} \tag{9}$$

For $\phi \equiv 1$, the requirement $\bar{\phi} = 1$ leads to a consistency condition that is discussed in Subsection 2.2.3.

The equation of state (Eq. (3)) for the particle properties is

$$p^* = \rho^* \kappa^* \epsilon_s^*. \tag{10}$$

The velocity of the particle is

$$\mathbf{U}^*(t) = \tilde{\mathbf{U}}^* + \mathbf{u}^*(t), \tag{11}$$

that is, the sum of the local mean and the particle's fluctuation. The particles move, like fluid particles, with their own velocity

$$\frac{dX_j^*}{dt} = U_j^*, \tag{12}$$

and the other particle properties evolve in the same way as fluid-particle properties in ideal flow (in which the viscosity, thermal conductivity, and molecular diffusivity are zero):

$$\frac{dU_j^*}{dt} = -\frac{1}{\rho^*} \left(\frac{\partial p}{dx_j} \right)^*, \tag{13}$$

$$\frac{dY_j^*}{dt} = S_j(\mathbf{Y}^*, p^*, T^*), \tag{14}$$

$$\frac{dh^*}{dt} = \frac{1}{\rho^*} \frac{dp^*}{dt}. \tag{15}$$

In the enthalpy equation, dp^*/dt denotes the rate of change of pressure following the particle.

Equations (10)–(15) fully describe the evolution of the particle properties and form a non-redundant system, i.e., none of them can be derived from the others. It is important to note that the other particle equations described below as well as all the mean field equations described in Subsection 2.2.2 are derived from these equations together with the auxiliary consistency conditions. (See the Appendix for the derivations.)

The fluctuating velocity is defined as

$$u_j^* = U_j^* - \tilde{U}_j^*, \tag{16}$$

and it evolves by (cf. the Appendix)

$$\frac{du_j^*}{dt} = -u_i^* \left(\frac{\partial \tilde{U}_j}{\partial x_i} \right)^* + \left(\frac{1}{\bar{\rho}^*} - \frac{1}{\rho^*} \right) \left(\frac{\partial p}{\partial x_j} \right)^* + \frac{1}{\bar{\rho}^*} \left(\frac{\partial}{\partial x_i} [\bar{\rho} \langle u_i^* u_j^* \mid \mathbf{x} \rangle] \right)^*. \tag{17}$$

Deduced from Eq. (15), the evolution equations for the sensible internal energy $\epsilon_s^* = h^* - p^* v^* - \sum_\alpha \epsilon_\alpha^{so} Y_\alpha^*$ and the sensible enthalpy $h_s^* = \epsilon_s^* + p^* v^*$ are given by

$$\frac{d\epsilon_s^*}{dt} = -p^* \frac{dv^*}{dt} + \dot{\epsilon}_s^*, \tag{18}$$

$$\frac{dh_s^*}{dt} = v^* \frac{dp^*}{dt} + \dot{\epsilon}_s^*, \tag{19}$$

where ϵ_α^{so} is defined by Eq. (67) in the Appendix and

$$\dot{\epsilon}_s^* = -\sum_\alpha \epsilon_\alpha^{so} \frac{dY_\alpha^*}{dt}. \tag{20}$$

Note that the mean quantities appearing in the particle evolution equations are interpolated from the corresponding particle or mean fields on the particle position, for instance, $\bar{\rho}^*(t) \equiv \bar{\rho}(\mathbf{X}^*[t], t)$. It is emphasized here that, contrary to the PDF equations, the particle evolution equations of the stochastic ideal flow are not stochastic.

2.2.2. Finite volume system. The system of equations solved by the FV method is directly derived from the particle evolution equations and the particle equation of state so that it is completely consistent with the particle system. For the reacting stochastic ideal flow, the conservation equations for the mean mass and momentum derived in the Appendix are

$$\frac{\partial \bar{\rho}}{\partial t} + \frac{\partial}{\partial x_i}(\bar{\rho}\tilde{U}_i) = 0, \tag{21}$$

$$\frac{\partial}{\partial t}(\bar{\rho}\tilde{U}_j) + \frac{\partial}{\partial x_i}[\bar{\rho}\tilde{U}_i\tilde{U}_j + p\delta_{ij}] = R_j, \tag{22}$$

where

$$R_j = -\frac{\partial}{\partial x_i}[\bar{\rho}\langle u_i^* u_j^* \mid \mathbf{x}\rangle]. \tag{23}$$

The energy variable used is the total sensible energy $\tilde{e}_s$ defined as

$$\tilde{e}_s = \bar{\rho}\left(\tilde{\epsilon}_s + \frac{1}{2}\tilde{U}_i\tilde{U}_i\right), \tag{24}$$

which evolves by

$$\frac{\partial \tilde{e}_s}{\partial t} + \frac{\partial}{\partial x_i}[\tilde{U}_i(\tilde{e}_s + p)] = \tilde{\dot{e}}_s + p\frac{\partial \breve{U}_i}{\partial x_i} - \frac{\partial G_i}{\partial x_i} + \tilde{U}_i R_i, \tag{25}$$

where

$$\tilde{\dot{e}}_s = -\bar{\rho}\sum_\alpha \epsilon_\alpha^{so}\left\langle \frac{dY_\alpha^*}{dt} \,\middle|\, \mathbf{x}\right\rangle, \tag{26}$$

$$G_i = \bar{\rho}\langle u_i^* \epsilon_s^* \mid \mathbf{x}\rangle, \tag{27}$$

$$\breve{U}_i = \tilde{U}_i - \bar{U}_i. \tag{28}$$

Finally the FV system is closed by the mean equation of state given by

$$p = \breve{\kappa}\left(\tilde{e}_s - \frac{1}{2}\bar{\rho}\tilde{U}_i\tilde{U}_i\right), \tag{29}$$

where

$$\breve{\kappa} = \frac{\langle \kappa^*\epsilon_s^* \mid \mathbf{x}\rangle}{\langle \epsilon_s^* \mid \mathbf{x}\rangle}. \tag{30}$$

As can be seen from the field equations (Eqs. (21), (22), and (25)), the terms on the left-hand side are in the same form as the compressible Euler equations while, as far as the FV method is concerned, the terms on the right-hand side do not contain time derivatives, and they are all supplied by the particle algorithm. Therefore, these equations may be considered as the compressible Euler equations with added source terms.

2.2.3. Consistency conditions. The mean density and the mean sensible internal energy are represented as duplicate fields which, together with the requirements that mean fluctuating velocity be zero and the particle volume be equal to the geometric volume occupied, raise the question of consistency. Since all the equations stem from a consistent, non-redundant set of equations, namely the particle equations (Eqs. (11)–(15)) and the particle equation of state (Eq. (10)), the present hybrid method is completely consistent at the equations level; i.e., the exact solutions of the equations yield identical duplicate fields. However, the consistency conditions may not be fulfilled at the level of numerical solutions depending on the accuracy of the numerical solution algorithms.

The conditions that need to be satisfied for consistency are

$$\langle \mathbf{u}^* \mid \mathbf{x}\rangle = 0, \tag{31}$$

$$\langle \epsilon_s^* \mid \mathbf{x}\rangle = (\tilde{\epsilon}_s)_{FV}, \tag{32}$$

$$(\bar{\rho})_P = (\bar{\rho})_{FV}, \tag{33}$$

$$\langle m^* v^* \delta(\mathbf{X}^* - \mathbf{x})\rangle = 1, \tag{34}$$

where the subscripts *FV* and *P* denote the FV and particle fields, respectively. It is emphasized that these conditions are not all independent. For $\phi \equiv 1$, Eq. (9) yields

$$\langle m^* v^* \delta(\mathbf{X}^* - \mathbf{x})\rangle = \langle v^* \mid \mathbf{x}\rangle(\bar{\rho})_P = 1. \tag{35}$$

The particle equation of state (Eq. (9)) is $v^* = \kappa^*\epsilon_s^*/p^*$. Thus

$$\begin{aligned}\langle m^* v^* \delta(\mathbf{X}^* - \mathbf{x})\rangle &= \left\langle \frac{m^*\kappa^*\epsilon_s^*}{p^*}\delta(\mathbf{X}^* - \mathbf{x})\right\rangle \\ &= \frac{\langle \kappa^*\epsilon_s^* \mid \mathbf{x}\rangle}{p}(\bar{\rho})_P \\ &= \frac{(\bar{\rho})_P}{p}\breve{\kappa}\langle \epsilon^* \mid \mathbf{x}\rangle,\end{aligned} \tag{36}$$

where Eq. (30) has been used. Substituting Eq. (36) and the FV equation of state $p = \breve{\kappa}(\bar{\rho})_{FV}(\tilde{\epsilon}_s)_{FV}$ into Eq. (35) results in

$$\langle v^* \mid x\rangle(\bar{\rho})_P = \frac{(\bar{\rho})_P}{(\bar{\rho})_{FV}} \frac{\langle \epsilon_s^* \mid \mathbf{x}\rangle}{(\tilde{\epsilon}_s)_{FV}} = 1. \tag{37}$$

Equations (36) and (37) imply that Eqs. (31) and (32) are the only independent consistency conditions at the level of numerical solutions. For if these are satisfied, Eq. (37) yields

$$(\bar{\rho})_P = (\bar{\rho})_{FV}, \tag{38}$$

and it then follows from Eqs. (35) and (37)

$$\langle m^* v^* \delta(\mathbf{X}^* - \mathbf{x})\rangle = 1. \tag{39}$$

In summary: the method is completely consistent at the level of the partial differential equations. That is, the exact solutions to these equations yield identical duplicate fields. At the level of the numerical solutions, there are just two independent conditions that ensure the consistency of the method, namely Eqs. (31) and (32).

3. NUMERICAL METHODS

3.1. *Coupled FV/Particle Algorithm*

The FV and particle methods are periodically used in the hybrid algorithm to solve their respective equations. Each period is called an "outer" iteration which consists of FV and particle "inner" iterations. The hybrid FV/particle algorithm can be designed to run in a tightly or loosely coupled manner. In this study, a loosely coupled algorithm has been adopted in which an outer iteration is completed by running the FV code until convergence and the particle code for a specified number of time steps. Note that tight coupling, in which both the FV and particle codes are run for a single time step to complete an outer iteration, is in fact a special case of loose coupling. Tight coupling is useful if time accuracy is desired: but we are interested here only in statistically steady solutions.

The early outer iterations produce a noisy solution close to a statistically stationary state and the subsequent iterations are performed to reduce the noise. As will be discussed later in detail, time-averaging is an effective way to reduce the statistical fluctuations in the particle fields when it is applied during a statistically stationary state. Therefore time-averaging is not performed until the outer iteration is deemed to be close to a statistically stationary state, say, at the k_oth outer iteration. The total number of time steps to be performed in the particle code during kth outer iteration is then determined according to

$$N_{TA}^{(k)} = \begin{cases} M_0 & \text{if } k < k_o \\ \beta^{k-k_0} M_{TA} & \text{if } k \geq k_o, \end{cases} \tag{40}$$

where M_0, β, and M_{TA} are positive constant parameters, taken in the present study as 20, 2.0, and 8, respectively, unless specified otherwise. Note that, in each outer iteration with $k \geq k_o$, the time-averaging is based on just the $N_{TA}^{(k)}$ particle time steps performed in that outer iteration.

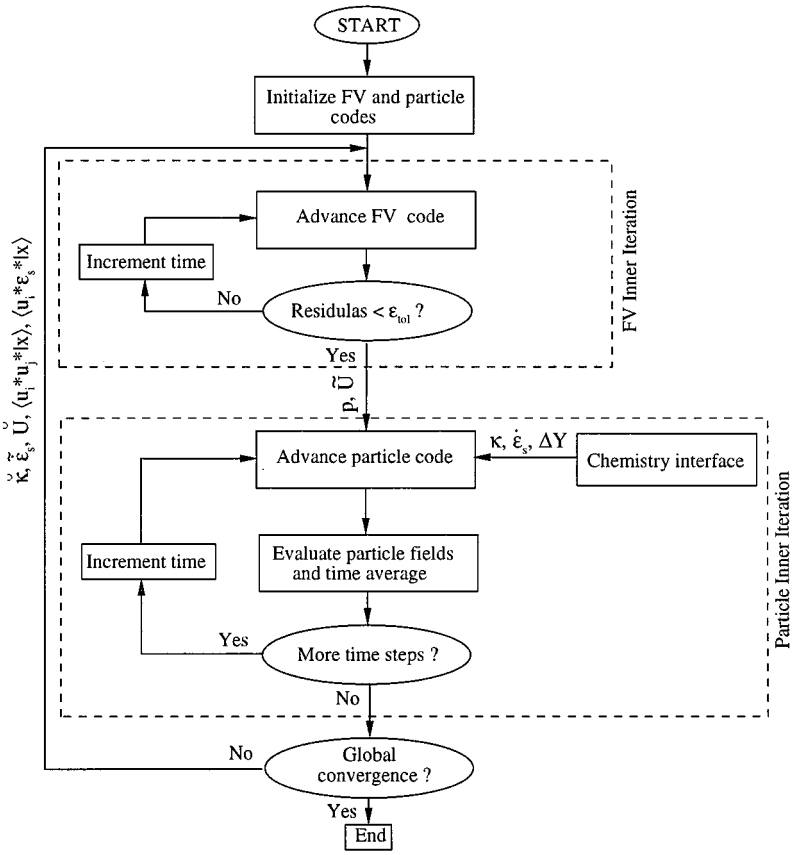

FIG. 1. Flow chart of the hybrid FV/particle method.

The overall solution sequence can be summarized as follows. The FV code is run until residuals are decreased to a specified tolerance value (ϵ_{tol}) and the required mean fields are passed to the particle code. The particle code is then run for a certain number of time steps (cf. Eq. (40)) and the necessary quantities are transferred back to the FV code. This process is repeated until global convergence is attained. The issue of the global convergence is discussed in Subsection 4.3 in detail. The flow chart for the hybrid algorithm is shown in Fig. 1.

3.2. *Finite Volume (FV) Method*

As mentioned earlier, the field equations solved by the FV method are of the same form as the compressible Euler equations with added source terms, so they can be solved by established techniques such as time-marching algorithms. In this paper, we employ a diagonalized implicit scheme based on that of Caughey [23] with a local preconditioning method developed by Muradoglu and Caughey [24]. The preconditioning is needed to remove the well known numerical difficulties due to eigenvalue stiffness caused by the large disparity between the characteristic wave speeds at low Mach numbers [25]. The details of the diagonalized implicit scheme and the preconditioning method can be found in Muradoglu and Caughey [24].

The source terms in the mean energy equation (Eq. (25)) can introduce an additional stiffness causing the numerical algorithm to be unstable unless an extremely small time step is used. The point implicit method developed by Bussing and Murman [27] has proven to be an effective way to remove the time step restriction set by stiff source terms. However, since the source terms in the mean field equations are not known as functions of the dependent variables, exact linearizations for use in the point implicit method is not possible. Therefore, a technique similar to that devised by Palmer [26] has been developed to overcome the stiffness problem without implicit treatment of the source terms. Motivated by the observation that large source terms compared to the convective fluxes can cause non-physical zero or negative values of density that lead to instabilities, the method is designed to limit the rate of change in density and not to allow non-physical solutions. The algorithm is as follows:

(i) obtain the increment in density field $\delta\rho$ from solution of the continuity equation;

(ii) find the maximum increment in absolute values $|\delta\rho|_{max}$ over the entire field, and if it is larger than a prescribed tolerance, i.e., $\alpha_\rho \rho_{ref}$, scale the increments as

$$\delta\rho = \frac{\delta\rho}{|\delta\rho|_{max}} \alpha_\rho \rho_{ref}, \tag{41}$$

where ρ_{ref} is the reference density and α_ρ is a prescribed constant typically taken as 0.01;

(iii) update the density

$$\rho^{n+1} = \max\left(\epsilon_\rho \cdot \rho_{ref}, \rho^n + \delta\rho\right), \tag{42}$$

where ϵ_ρ is a small positive number with typical value 0.005.

This method prevents wild swings in the density field and allows the solution to relax smoothly to the steady-state. Our numerical experience shows that this simple procedure maintains stability of the numerical algorithm even for very large source terms, e.g., corresponding to maximum density ratio as large as 25.

The boundary conditions are specified as follows. The mean velocity and density at the inlet and the pressure at the outlet are fixed to the physical values while the pressure at the inlet and the mean velocity and density at the outlet are extrapolated from the computational domain. This treatment is consistent with the characteristic theory since we are interested here only in subsonic flows.

This FV scheme accepts both a uniform or non-uniform grid but a uniform grid is used in the present study for simplicity.

3.3. *Particle Method*

The particle method described here is developed to solve the particle equations in the context of the hybrid algorithm. In this method, fluid particles are modeled by an ensemble of notional particles which are distributed in the physical space and carry the intrinsic properties mass m^*, position $\mathbf{X}^*$, fluctuating velocity $\mathbf{u}^*$, mass fractions $\mathbf{Y}^*$, and enthalpy h^*. The computational domain is overlaid by a uniform or non-uniform spatial grid for the purpose of estimating the particle fields from the particle properties and interpolating the FV and particle fields onto the particles as needed in the solution of the particle equations. The particle fields are required to close the FV and particle equations as well as to represent the numerical results. In the present study, the particle fields are estimated from the particle properties by a non-parametric kernel estimation method based on linear basis functions.

This is a cloud-in-cell (CIC) method [31] in which the particle fields on each grid node are approximated as weighted ensemble of the particles in the neighboring cells of the node. The details of the method can be found in [32]. The mean quantities at the particle positions are interpolated from the nodal values of the corresponding FV or particle fields using linear splines. Note that the spatial derivatives appearing in the particle equations are first evaluated at the nodes using second order central differences and then interpolated on the particle locations. It is emphasized that the FV mean field derivatives, for example, $\partial \tilde{U}_i/\partial x_j$, are evaluated consistently with the way the same derivatives are treated in the FV code. The kernel estimation, evaluation of the spatial derivatives, and interpolation schemes are all second order accurate yielding second order accuracy in space. In this work, the same grid is used both in the FV and particle methods but this is not required in general.

The system of particle evolution equations is integrated forward in time using a multistep, second order scheme. Each particle moves at its own velocity

$$\frac{dX_i^*}{dt} = \tilde{U}_i^* + u_i^*, \tag{43}$$

and defining $\mathbf{Q_P}(\mathbf{x}, t)$ and $\mathbf{Q_{FV}}(\mathbf{x}, t)$ as the particle and FV fields, respectively, all the other particle equations (Eqs. (12), (14), (17), and (19)) can be written in vector form as

$$\frac{d\phi_i^*(t)}{dt} = S_{\phi_i}(\mathbf{X}^*(t), \phi^*(t), \mathbf{Q_P}(\mathbf{X}^*[t], t), \mathbf{Q_{FV}}(\mathbf{X}^*[t], t)), \tag{44}$$

where ϕ_i^* is the vector of the dependent variables and S_{ϕ_i} is the vector representing the source terms on the right hand-side of the particle equations. Note that the mean density and Reynolds stresses are the only particle fields used in the particle equations since the mean velocity and pressure are provided by the FV method.

In advancing the particle properties from time level $n(t_n = n\Delta t)$ to level $n+1$, the solutions at time $t_{n+1/2} = \frac{1}{2}(t_n + t_{n+1})$ are first predicted using the explicit Euler method

$$X_i^{*n+1/2} = X_i^{*n} + \frac{\Delta t}{2}\left(\tilde{U}_i^{*n} + u_i^{*n}\right), \tag{45}$$

$$\phi_i^{*n+1/2} = \phi_i^{*n} + \frac{\Delta t}{2} S_{\phi_i}^{*n}, \tag{46}$$

where $S_{\phi_i}^{*n}$ is written for $S_{\phi_i}^{*n} = S_{\phi_i}(\mathbf{X}^{*n}, \phi^{*n}, \mathbf{Q}_\mathbf{P}^{*n}, \mathbf{Q}_\mathbf{FV}^{*n})$. In this intermediate step, $\mathbf{Q}_\mathbf{P}^{*n+1/2}$ and $\mathbf{Q}_\mathbf{FV}^{*n+1/2}$ are also evaluated by interpolating the corresponding FV and particle fields on the predicted particle positions.

In the next step, all the particle equations except for the convection are integrated to yield the new particle properties using the midpoint rule

$$\phi_i^{*n+1} = \phi_i^{*n} + \Delta t S_{\phi_i}^{*n+1/2}, \tag{47}$$

and the new particle position is subsequently calculated as

$$\begin{aligned} X_i^{*n+1} &= X_i^{*n} + \frac{\Delta t}{2}\left(u_i^{*n} + u_i^{*n+1}\right) + \Delta t \tilde{U}_i^{*n+1/2}, \\ &= X_i^{*n+1/2} + \frac{\Delta t}{2}\left(2\tilde{U}_i^{*n+1/2} - \tilde{U}_i^{*n}\right) + \frac{\Delta t}{2} u_i^{*n+1}, \end{aligned} \tag{48}$$

where Eq. (45) has been used. Notice that convection due to the mean and the fluctuating velocities are evaluated by the midpoint and the trapezoidal methods, respectively.

Finally the particle fields are evaluated using the kernel estimation method based on the particle properties at the new time level and then the mean quantities are interpolated on the new particle locations to obtain $\mathbf{Q}_{\mathbf{P}}^{*n+1}$ and $\mathbf{Q}_{\mathbf{FV}}^{*n+1}$. The overall scheme consists of a combination of midpoint and trapezoidal methods yielding second order accuracy in time.

4. RESULTS AND DISCUSSION

4.1. *Test Problem*

Numerical properties of the hybrid method have been studied through 1D reacting stochastic ideal flows of a premixed methane–air mixture in a constant-area channel, as sketched in Fig. 2. The stoichiometric gas mixture enters the channel at high temperature and combustion occurs by auto-ignition.

As far as the thermochemistry is concerned, variations in pressure are negligible compared to the pressure itself. Hence the enthalpy h is conserved, and the mass fractions $\mathbf{Y}$ depend solely on residence time t_r (see Eqs. (14) and (15)). Thus all the thermodynamic variables can be pre-calculated and tabulated as function of the residence time.

The methane–air combustion mechanism employed here consists of 16 species and 41 reactions [28]. The species conservation equations are solved separately using the CHEMKIN library [29] and a look-up table is formed for the quantities κ, the rate of change in the sensible internal energy $\dot{\epsilon}_s$, the sensible internal energy ϵ_s, and the density ρ as functions of the residence time t_r. The first two quantities, κ and $\dot{\epsilon}_s$, are then interpolated on the particles as needed in the particle equations while ϵ_s and ρ are used for comparison with those computed by the particle and FV methods.

The time steps taken in the FV and particle methods are specified through CFL numbers. The CFL number in the FV method is defined in the usual way as

$$(CFL)_{FV} = \max_i \left| \frac{\lambda_i \Delta t_{FV}}{\Delta x} \right|, \tag{49}$$

where λ_i, Δt_{FV}, and Δx are the characteristic wave speeds corresponding to the preconditioned system of the field equations, the time step taken in the FV method and the characteristic mesh interval, respectively. In a similar way, the particle CFL number is defined as

$$(CFL)_P = \frac{|\tilde{U}|_{\max} \Delta t_P}{\Delta x}, \tag{50}$$

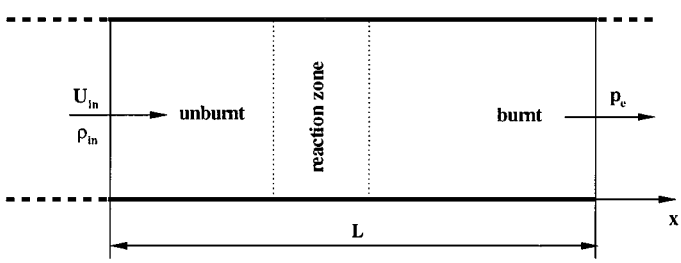

FIG. 2. Sketch of 1D reacting stochastic ideal flow.

where $\tilde{U}_{\max}$ and Δt_P are the maximum mean velocity in magnitude and the time step used in the time-integration scheme for the particle equations.

In all the results presented here, the boundary conditions are specified as follows. At the inlet boundary, the mean velocity, density, and temperature are set equal to $\tilde{U}_{in} = 10.40$ m/s, $\bar{\rho}_{in} = 0.2448\,\text{kg/m}^3$, and $\tilde{T}_{in} = 1500^\circ$K and the fluctuating velocity pdf is Gaussian with mean $\langle u \rangle_{in} = 0$ and variance $\langle u^2 \rangle_{in} = 1.0\,\text{m}^2/\text{s}^2$. Thus the rms velocity fluctuation is about 9.6% of the mean velocity at the inlet. At the exit boundary, the pressure is fixed at $P_e = 101{,}325$ Pa. Note that the specified density $\bar{\rho}_{in}$ corresponds to the density of the stoichiometric methane–air mixture at temperature $\tilde{T}_{in}$ and pressure P_e. The length of the channel is chosen to be $L = 0.04$ m. At the beginning of the simulation, the particles are randomly distributed in physical space and the particle properties are initialized to yield the particle fields equal to the inlet boundary conditions. The particle masses, m^*, are initialized in such a way that the total mass of the particles in each cell is equivalent to the mass of the fluid in the cell occupied. The mean fields in the FV method are initially set equal to the non-reacting uniform flow corresponding to the boundary conditions.

Figures 3 and 4 show stationary distributions of the mean density and the mean sensible internal energy, respectively. For the simulation, the computational domain is divided into $N_x = 128$ equal cells and initially $N_{pc} = 40$ particles are randomly distributed in each cell. The CFL numbers in the FV and particle methods are fixed at $(CFL)_{FV} = 8.0$ and $(CFL)_P = 0.3$, respectively. After reaching a stationary solution, time-averaging is performed over $N_{TA} = 64000$ time steps taken in the particle code to get smooth solutions. The details of the time-averaging method will be discussed later. Since the mean density and sensible internal energy are represented as duplicate fields, the FV and particle solutions should agree for consistency. As can be seen in these figures, the remarkable agreement between the FV and particle fields confirms that the consistency conditions are well satisfied in the present hybrid method at the level of numerical solution. The small differences observed between the FV and particle solutions are mainly due to lack of grid resolution in the FV method. The fields $\bar{\rho}_{Ch}$ and $(\tilde{\epsilon}_s)_{Ch}$ plotted in the figures are obtained from the

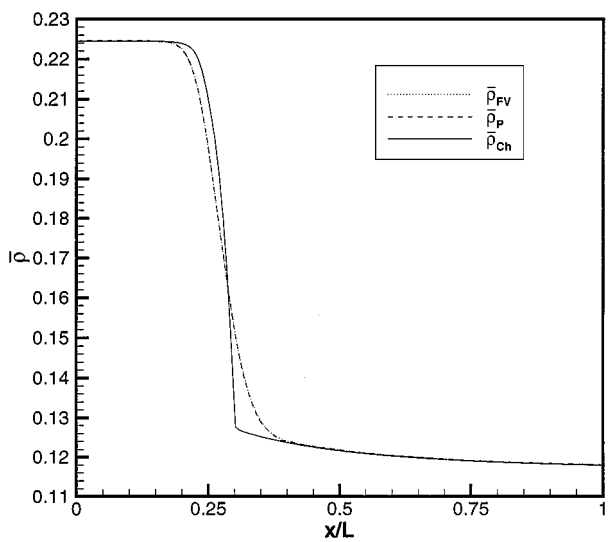

FIG. 3. Stationary distribution of the mean density $\bar{\rho}$. $N_{pc} = 40$, $N_x = 128$, $N_{TA} = 64000$, $(CFL)_P = 0.3$, and $(CFL)_{FV} = 8.0$.

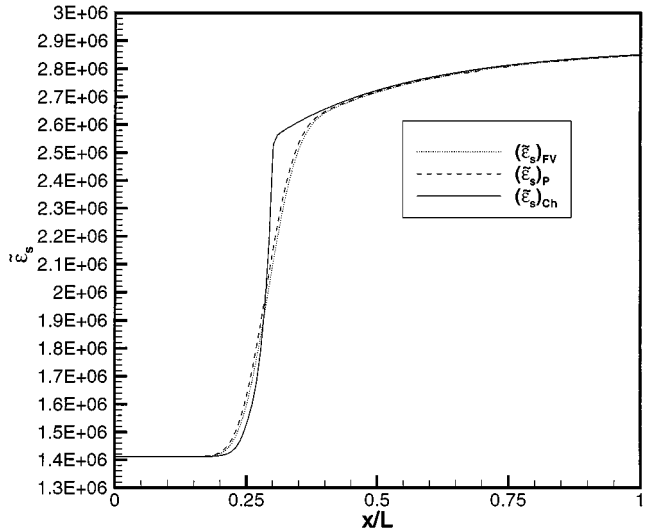

FIG. 4. Stationary distribution of the mean sensible internal energy $\tilde{\varepsilon}_s$. $N_{pc} = 40$, $N_x = 128$, $N_{TA} = 64000$, $(CFL)_P = 0.3$, and $(CFL)_{FV} = 8.0$.

chemistry model based on the mean residence time defined as

$$\tilde{t}_r = \int_0^x \frac{dx}{\tilde{U}(x)}, \tag{51}$$

where $\tilde{U}(x)$ is the mean velocity. Hence these fields are not expected to agree with the FV and particle solutions.

For the same case, the scatter plot of the fluctuating velocity and the stationary distribution of $\langle u^{*2} \mid x \rangle$ are depicted in Figs. 5 and 6, respectively. These figures indicate that the variance of the fluctuating velocity decreases considerably in the reaction zone mainly due to large

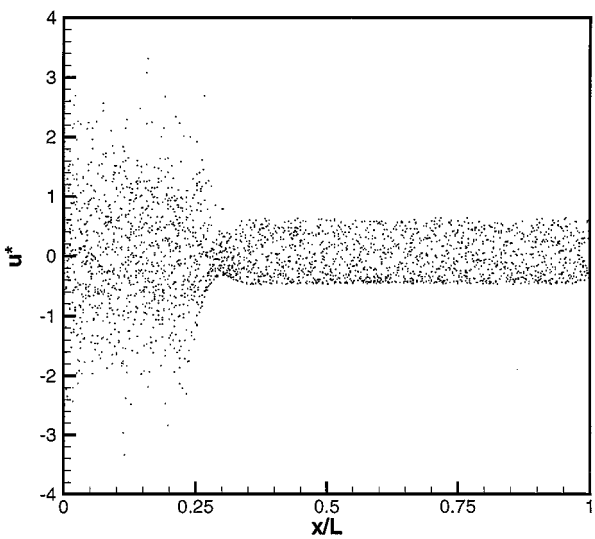

FIG. 5. Scatter plot of the fluctuating velocity u. $N_{pc} = 40$, $N_x = 128$, $N_{TA} = 64000$, $(CFL)_P = 0.3$, and $(CFL)_{FV} = 8.0$.

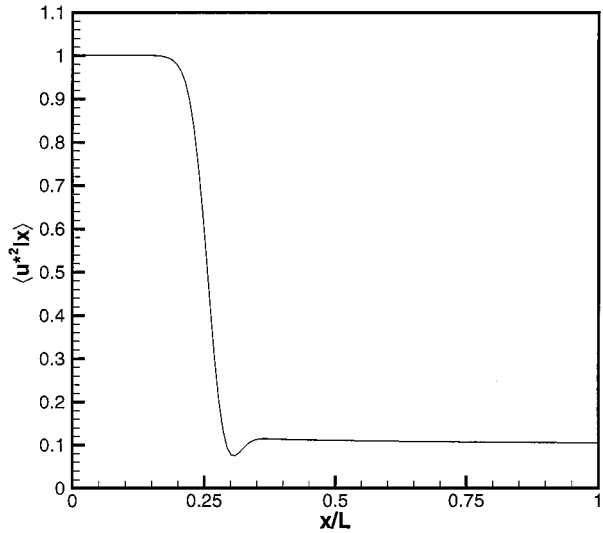

FIG. 6. Stationary distribution of $\langle u^{*2} \mid x \rangle$. $N_{pc} = 40$, $N_x = 128$, $N_{TA} = 64000$, $(CFL)_P = 0.3$, and $(CFL)_{FV} = 8.0$.

positive mean velocity gradient present in this region. In the particle equations (cf. Eq. (17)), this effect is represented by the term

$$\frac{du_j^*}{dt} = -u_i^* \left(\frac{\partial \tilde{U}_j}{\partial x_i} \right)^* + \cdots. \tag{52}$$

The apparent preponderance of particles near a sharp lower bound in u^* space in Fig. 5 is due to the fact that the particles with negative fluctuating velocity experience the positive mean velocity gradient longer than those with the positive fluctuating velocity. Therefore, the magnitude of the negative fluctuating velocity is more reduced than that of the positive fluctuating velocity.

It is found that the consistency condition expressed by Eq. (31) is satisfied sufficiently well so that no correction is performed on the fluctuating velocity. For the particular case shown in Fig. 5, for instance, the magnitude of the mean fluctuating velocity normalized by its rms value, $\langle u^* \mid x \rangle / u'$, remains smaller than 10^{-3} everywhere.

4.2. *Numerical Errors*

The purpose of this subsection is to identify and to quantify the various numerical errors that arise in the hybrid method due to finite values of the number of particles per cell N_{pc}, the time step taken in the time-integration scheme for the particle equations Δt_P, and the characteristic cell size Δx. Note that since a steady-state is reached, the time step taken in the FV method has no effect on the final solution. Therefore, the only time-stepping error comes from the finite time step taken in the particle method.

In stochastic methods, convergence of numerical algorithms can be interpreted in either a strong or a weak sense [33]. Weak convergence requires convergence of mean quantities obtained by the numerical method to the actual means rather than the convergence of the particle properties as needed for strong convergence. Since mean quantities are of essential interest rather than individual sample paths, it is appropriate to seek weak convergence in

this hybrid method. When estimating a mean quantity $\langle Q\rangle$ at a fixed position and time in a numerical simulation with N_{pc} particles per cell, time step taken in the particle algorithm Δt_p, and characteristic cell size Δx, the numerical error in the estimated mean denoted by $\{Q\}_{N_{pc},\Delta x,\Delta t_p}$ is a random variable and can be decomposed as

$$\epsilon_Q \equiv \{Q\}_{N_{pc},\Delta x,\Delta t_p} - \langle Q\rangle = \Sigma_Q + D_Q = \Sigma_Q + B_Q + H_Q + T_Q, \tag{53}$$

where Σ_Q and D_Q are the statistical and the deterministic errors, respectively. The deterministic errors are further broken into the bias B_Q, the spatial error H_Q, and the temporal error T_Q. The statistical error arises from the random inlet boundary conditions in the particle method. The bias is the deterministic error caused by the statistical fluctuations in the particle fields used in the particle evolution equations [30]. The spatial error results from the spatial discretization of the field equations in the FV method, as well as, from the kernel estimation and interpolation in the particle method. As mentioned earlier, the temporal error is solely due to finite time step used in the time-integration scheme for the particle equations. These four types of errors are studied and quantified individually. Note that all the errors are normalized by the reference values for the corresponding particle and FV fields.

4.2.1. Statistical error. The statistical error in the estimated particle field $\{Q\}_{N_{pc},\Delta x,\Delta t_p}$ is given by

$$\Sigma_Q = \{Q\}_{N_{pc},\Delta x,\Delta t_p} - \left\langle \{Q\}_{N_{pc},\Delta x,\Delta t_p}\right\rangle \tag{54}$$

and it is measured by its standard error defined as

$$S_Q = \left[N_{pc}\mathrm{var}\left(\{Q\}_{N_{pc},\Delta x,\Delta t_p}\right)\right]^{1/2}. \tag{55}$$

The rms statistical error σ_Q is therefore $N_{pc}^{-1/2}S_Q$. As N_{pc} approaches infinity, S_Q becomes independent of N_{pc} so that the rms statistical error scales as $N_{pc}^{-1/2}$.

Table II shows the dependence of the standard error on N_{pc} for the particle fields $\bar{\rho}_P$, $(\tilde{\epsilon}_s)_P$, $\tilde{u}$, and $\langle u^{*2}\,|\,x\rangle$. In evaluating the standard error, the variance of each quantity is estimated along the length of the channel from 4000 samples and averaged over all the grid points in the domain. Instead of different independent trials, the samples are obtained from the solutions at consecutive time steps during the stationary state. The parameter N_{pc} is varied from 20 to 640. It is observed that the statistical error is significantly larger in $\tilde{u}$ and $\langle u^{*2}\,|\,x\rangle$ than in $\bar{\rho}_P$ and $(\tilde{\epsilon}_s)_P$ but the standard error remains approximately constant for each of the quantities showing the expected scaling.

TABLE II
The Standard Error versus Number of Particles per Cell

N_{pc}	$S_{\bar{\rho}P}$	$S_{(\tilde{\epsilon}_s)_P}$	$S_{\tilde{u}}$	$S_{\langle u^{*2}\,\vert\,x\rangle}$
20	2.16×10^{-2}	4.91×10^{-2}	5.88×10^{-1}	4.75×10^{-1}
40	2.27×10^{-2}	5.20×10^{-2}	5.86×10^{-2}	4.69×10^{-1}
80	2.14×10^{-2}	4.94×10^{-2}	5.66×10^{-2}	4.49×10^{-1}
160	2.13×10^{-2}	4.93×10^{-2}	5.57×10^{-2}	4.49×10^{-1}
320	2.11×10^{-2}	4.90×10^{-2}	5.62×10^{-2}	4.38×10^{-1}
640	2.09×10^{-2}	4.89×10^{-2}	5.50×10^{-2}	4.27×10^{-1}

TABLE III
The rms Statistical Error Times $N_{TA}^{1/2}$ versus N_{TA}

N_{TA}	$N_{TA}^{1/2}\sigma_{\bar{\rho}P}$	$N_{TA}^{1/2}\sigma_{\bar{u}}$	$N_{TA}^{1/2}\sigma_{\langle u^{*2}\mid x\rangle}$
32	2.22×10^{-2}	4.88×10^{-1}	9.62×10^{-1}
128	1.79×10^{-2}	6.29×10^{-1}	9.91×10^{-1}
512	1.44×10^{-2}	5.74×10^{-1}	8.36×10^{-1}
2048	1.76×10^{-2}	6.96×10^{-1}	8.09×10^{-1}
8192	2.12×10^{-2}	4.79×10^{-1}	9.21×10^{-1}
32768	2.39×10^{-2}	6.57×10^{-1}	10.00×10^{-1}

Due to the slow convergence of the statistical error with N_{pc}, the required number of particles increases dramatically as the desired error level is decreased and quickly becomes computationally prohibitive. For example, while it requires only about 100 particles per cell to achieve an overall rms statistical error level of 5%, N_{pc} must be increased to 2500 to reduce the error to level of 1%. However, instead of increasing the number of particles, the statistical error can be reduced through a time-averaging procedure. If N_{TA} time steps are taken in the particle code during an outer loop after reaching a stationary solution, the time-averaged mean for $\{Q\}_{N_{pc},\Delta x,\Delta t_p}$ is defined as

$$\left\langle \{Q\}_{N_{pc},\Delta x,\Delta t_p}\right\rangle_{N_{TA}} \equiv \frac{1}{N_{TA}}\sum_{n=1}^{N_{TA}}\{Q\}^{(n)}_{N_{pc},\Delta x,\Delta t_p}. \tag{56}$$

Thus, for large N_{TA}, the rms statistical error in the time-averaged field scales as $(N_{pc}N_{TA})^{-1/2}$.

Table III presents the rms statistical error σ_Q times $N_{TA}^{1/2}$ against N_{TA} for the particle fields $\bar{\rho}_P$, $\tilde{u}$, and $\langle u^{*2}\mid x\rangle$ over the range N_{TA} between 32 and 32,768. As can be seen in the table, $N_{TA}^{1/2}\sigma_Q$ remains approximately constant over this range indicating the expected scaling of the rms statistical error with N_{TA}. In the table, σ_Q is estimated from 100 statistically independent simulations and averaged over the entire computational domain. All the calculations are performed for the fixed parameters $N_{pc}=10$, $N_x=128$, $(CFL)_P=0.3$, and $(CFL)_{FV}=8.0$.

4.2.2. Bias. The bias is the deterministic error caused by N_{pc} being finite. As remarked earlier, the bias is one of the dominant errors in the self-contained particle method [12, 13]. Using the error decomposition in Eq. (53), the bias in the estimated particle field $\{Q\}_{N_{pc},\Delta x,\Delta t_p}$ can be written

$$B_Q = \left\langle \{Q\}_{N_{pc},\Delta x,\Delta t_p}\right\rangle - \{Q\}_{\infty,\Delta x,\Delta t_p}, \tag{57}$$

where $\{Q\}_{\infty,\Delta x,\Delta t_p} = \lim_{N_{pc}\to\infty}\{Q\}_{N_{pc},\Delta x,\Delta t_p}$. The main source of the bias is the statistical fluctuations in the particle fields used in the particle evolution equations. Both theoretical analysis and numerical experiments [30, 13] have shown that the bias scales as N_{pc}^{-1}.

In Fig. 7, the bias is plotted against N_{pc}^{-1} for the particle fields $\langle u^{*2}\mid x\rangle$ and $\bar{\rho}_p$ at the location $x/L=0.389$ over the range N_{pc} from 20 to 640. The approximate linear relationship between the bias and N_{pc}^{-1} confirms the expected inverse scaling. The bias is isolated as follows. The statistical error is kept small by fixing the product $N_{pc}N_{TA}=5.2\times10^6$ for which the overall rms statistical error is expected to be of order 2.2×10^{-4}. The bias-free

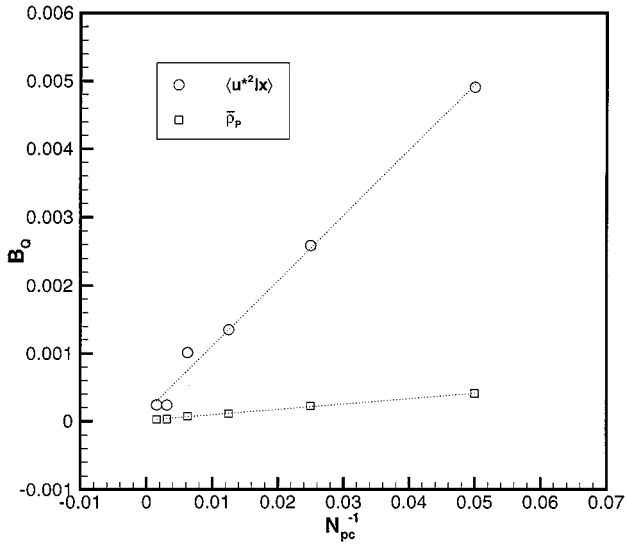

FIG. 7. Bias against N_{pc}^{-1} at $x/L = 0.389$. The number of particles per cell N_{pc} ranges from 20 to 640. The lines show linear-least-squares fits.

variable $\{Q\}_{\infty,\Delta x,\Delta t_p}$ is estimated by linear extrapolation in N_{pc}^{-1} to $N_{pc}^{-1} = 0$ using the values at $N_{pc} = 640$ and $N_{pc} = 1280$. Then the bias is calculated from Eq. (57). It is found that the maximum bias occurs in $\langle u^{*2} \mid x \rangle$. To give an idea about the distribution of the bias in the entire computational domain, it is plotted in Fig. 8 for $\langle u^{*2} \mid x \rangle$ along the channel. As can be seen in this figure, the bias is small, i.e., its maximum value is less than 1% even for $N_{pc} = 20$. This is an important result showing that the bias is not a dominant error in the hybrid method. Since the statistical error can be reduced effectively by time-averaging and the bias is small, it is possible to use many fewer particles in the hybrid method than in the self-contained particle algorithm to achieve a given level of accuracy.

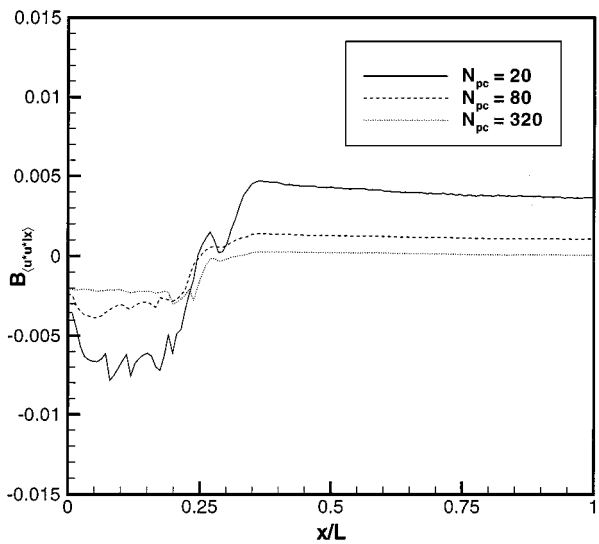

FIG. 8. Variation of bias in $\langle u^{*2} \mid x \rangle$ along the channel for various values of N_{pc}.

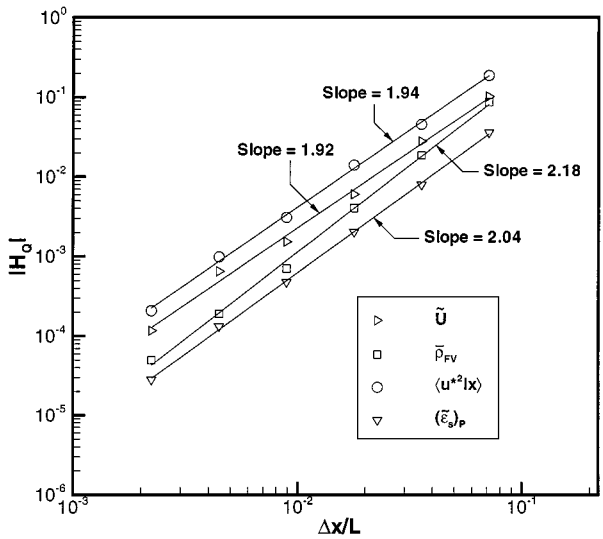

FIG. 9. Spatial error against $\Delta x/L$. The normalized cell size $\Delta x/L$ varies between 1/16 and 1/512. The slopes are obtained from linear-least-squares fits to each set of data.

4.2.3. Spatial error. The spatial error results from the spatial discretization in the FV method and also from the kernel estimation and interpolation in the particle algorithm. The spatial error in $\{Q\}_{N_{pc},\Delta x,\Delta t_p}$ is

$$H_Q = \{Q\}_{\infty,\Delta x,\Delta t_p} - \{Q\}_{\infty,0,\Delta t_p}, \tag{58}$$

where $\{Q\}_{\infty,0,\Delta t_p} = \lim_{N_{pc}\to\infty,\Delta x\to 0}\{Q\}_{N_{pc},\Delta x,\Delta t_p}$. The spatial discretization [23] and the kernel estimation and interpolation schemes [32] are all second order accurate, so the spatial error is expected to scale as Δx^2. This is verified in Fig. 9 for the selected mean and particle fields $\tilde{U}$, $\bar{\rho}_{FV}$, $\langle u^{*2}\,|\,x\rangle$, and $(\tilde{\epsilon}_s)_P$ over the range $\Delta x/L$ from 1/16 to 1/512 where L is the length of the channel. In all the simulations, the parameter N_{TA} is fixed at 10^4 and N_{pc} is varied to keep the total number of particles constant at $N_{pc}N_x = 1.28 \times 10^5$ which is equivalent to $N_{pc} = 1000$ for $N_x = 128$. Therefore, the rms statistical error and the bias are estimated to be of order 1.6×10^{-4} and 10^{-4}, respectively. Then $\{Q\}_{\infty,0,\Delta t_p}$ is estimated using Richardson extrapolation to the limit $\Delta x \to 0$. Thus the spatial error is obtained from Eq. (58) and averaged over the computational domain.

4.2.4. Temporal error. In this hybrid method, the sole source of the temporal error is the finite time steps taken in the time-integration scheme in the particle method. Since our interests lie in the steady-state solutions, the FV method does not contribute to the time-stepping error if it is fully converged. The temporal error T_Q in $\{Q\}_{N_{pc},\Delta x,\Delta t_p}$ is

$$T_Q = \{Q\}_{\infty,0,\Delta t_p} - \{Q\}_{\infty,0,0}, \tag{59}$$

where $\{Q\}_{\infty,0,0} = \lim_{N_{pc}\to\infty,\Delta x\to 0,\Delta t_p\to 0}\{Q\}_{N_{pc},\Delta x,\Delta t_p}$.

Figure 10 illustrates a log–log plot of the temporal error $|T_Q|$ against the time step taken in particle method for the particle fields $\langle u^{*2}\,|\,x\rangle$, $(\tilde{\epsilon}_s)_P$, and $\bar{\rho}_P$ over the range of the particle CFL number $(CFL)_P$ between 0.2 and 2.0. Note that the time step Δt_p is normalized by the average residence time T_r defined as the average time for a particle to travel

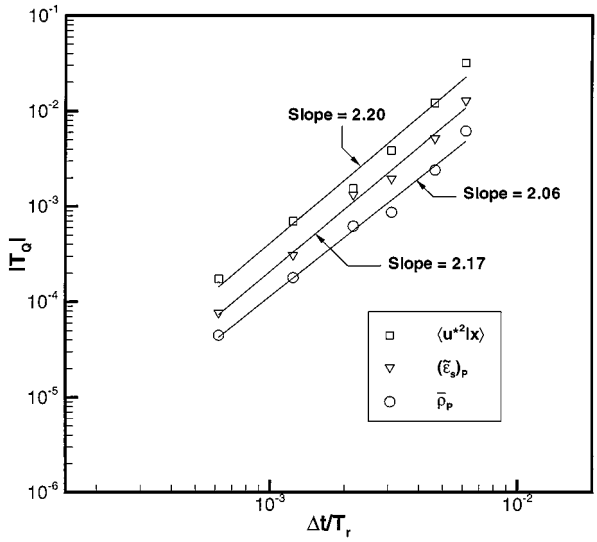

FIG. 10. Temporal error against $\Delta t_P / T_r$. The particle CFL number $(CFL)_P$ varies between 0.2 and 2.0. The slopes are obtained from linear-least-squares fits to each set of data.

from the inlet to the exit boundary. All the calculations are performed for the parameters $N_x = 256$, $N_{pc} = 500$, and $N_{TA} = 10^4$. Therefore, the bias and the rms statistical error are estimated to be of order 10^{-4} and 1.6×10^{-4}, respectively. The spatial error is predicted to be of order 2.4×10^{-3} which is larger than the smallest time-stepping error in the figure but the dominant effect of Δt_p is assumed to be through the temporal error T_Q. Richardson extrapolation is used to predict $\{Q\}_{\infty,0,0}$ in the limit as $\Delta t_P \to 0$. The slopes in the figure are obtained from linear-least-square fits and are found to be slightly larger but very close to the expected value 2.0 showing the second order accuracy of the time-integration scheme used to integrate the particle equations.

4.3. *Convergence*

The numerical errors have been discussed and quantified in the previous subsection, the convergence of the hybrid method will now be examined in detail. In a FV method, convergence is usually measured by residuals and a FV solution is considered to be converged when the magnitude of residuals is smaller than a specified tolerance value. In the hybrid method, however, a number of outer iterations are usually required to solve the flow field and the source terms appearing on the right hand side of the field equations are updated at the end of each outer iteration by passing the required particle fields from the particle code to the FV code. Even when a statistically stationary solution has been reached, the noisy particle fields feed back significant statistical fluctuations into the source terms and thus cause a jump in the convergence history of the FV solutions at the beginning of the inner FV iterations as shown in Fig. 11. The data in the figure are taken from a numerical simulation of 50 outer iterations with the parameters $N_{pc} = 40$, $N_x = 128$, $(CFL)_P = 0.3$, and $(CFL)_{FV} = 8.0$. Time-averaging is turned off throughout the simulation. An inner particle iteration of 20 time steps is performed between two adjacent FV cycles but it has not been displayed in the figure. Here the residual is defined as the mean of absolute residuals of the continuity, momentum, and energy equations averaged over the entire computational

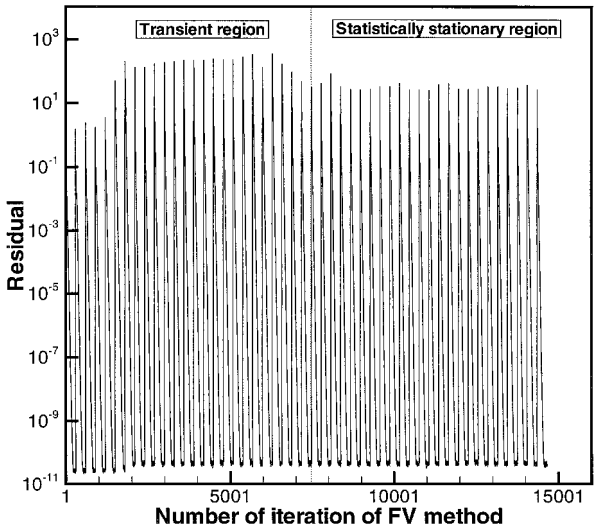

FIG. 11. Convergence history of the FV solutions over 50 outer iterations. $N_{pc} = 40$, $N_x = 128$, $(CFL)_P = 0.3$, and $(CFL) = 8.0$.

domain. As can be seen in this figure, the residual is quickly decreased to a small value in each FV cycle but the global convergence is not clearly shown even in the statistically stationary state. Similar results have also been observed in previous studies; see, e.g., Chang [15]. The residuals obtained at the beginning of the FV cycles are a good measure for the global convergence of the FV solutions and will hereafter be referred to as "initial residuals" or simply "residuals."

Since the jump in the convergence history is attributed to the statistical error in the source terms, the initial residuals may be expected to converge as $(N_{pc}N_{TA})^{-1/2}$. This is verified in Figs. 12 and 13 which show log–log plots of the initial residuals versus the number of particles per cell N_{pc} and the time-averaging parameter N_{TA}, respectively. The slopes

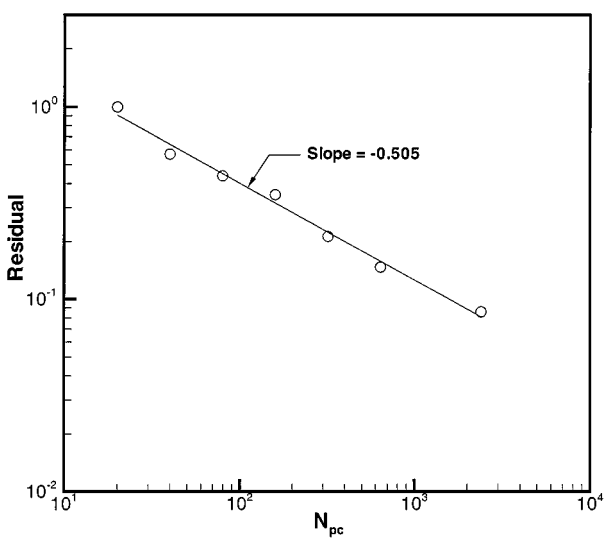

FIG. 12. Initial residual of FV solutions against N_{pc} without time-averaging. N_{pc} ranges from 20 to 2400. The slope is calculated from linear-least-squares fit.

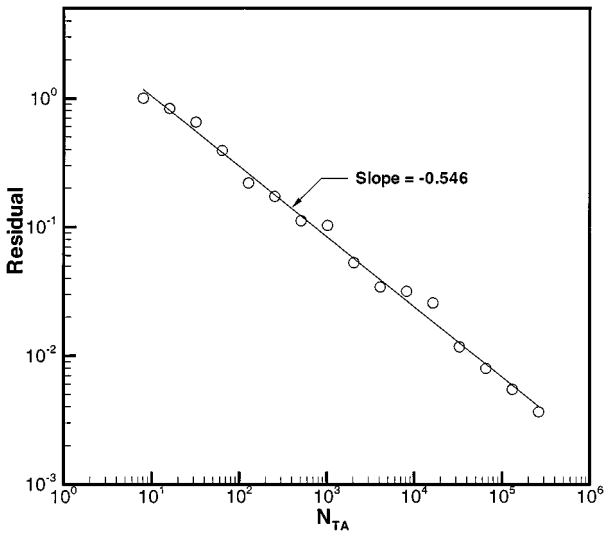

FIG. 13. Initial residual of FV solutions against N_{TA}. N_{TA} ranges from 8 to 262144 and $\beta = 2.0$. The slope is calculated from linear-least-squares fit.

of linear-least-square fits to each set of data are slightly smaller but very close to -0.5 that clearly illustrates the expected scaling. The data plotted in Fig. 12 are obtained from the statistically stationary solutions for N_{pc} ranging between 20 and 2400 and the other parameters are fixed at $N_x = 128$, $(CFL)_P = 0.3$, and $(CFL)_{FV} = 8.0$. Note that no time-averaging is applied in this case. In Fig. 13 on the other hand, all the parameters are kept the same as in Fig. 12 but the number of particles per cell is fixed at $N_{pc} = 40$ and the time-averaging is performed for various values of N_{TA} ranging between 8 and 262,144.

A log–log plot of the initial residuals against work units (WUs) is also displayed in Fig. 14 for the same case. (A work unit is defined here as the total computational labor required in advancing the particle code for a single time step. Note that the computational work done in

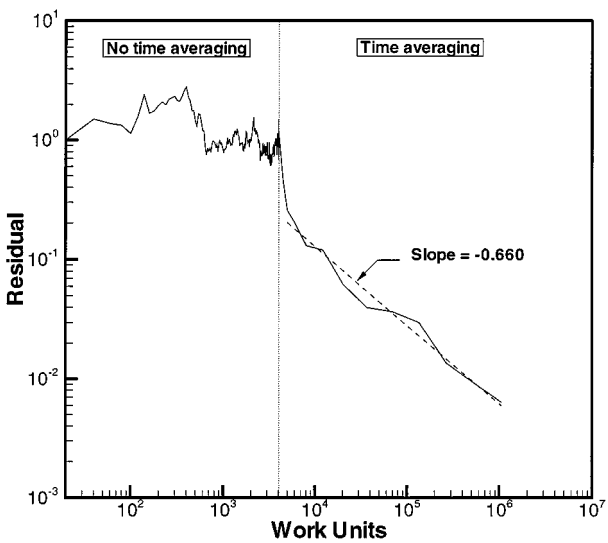

FIG. 14. Convergence history of initial residual of FV solutions. Time-averaging is started after 200 outer iterations with $\beta = 2.0$. The slope is calculated from linear-least-squares fit.

the FV code is neglected here since it accounts for less than 1% of the overall computational work in terms of CPU times.) This figure clearly shows the effect of the time-averaging on the global convergence of the FV solutions: the initial residuals remain approximately constant in the region where a statistically stationary solution is reached but no time-averaging is carried out, i.e., between WUs = 600 and WUs = 4000, and start decreasing immediately when the time-averaging is applied. It is assumed for this particular case that the stationary state $k > k_o$ is reached when all the initial particles leave the computational domain. The slope of the linear-least-square fit is found to be about -0.66 but it is expected to approach asymptotically to -0.5 as WU $\to \infty$.

It is difficult to measure the global convergence of the particle method since there are no corresponding residual as in the FV method. However, changes in the particle fields can be monitored for this purpose. The change in the particle field $\langle Q \rangle_P$ is defined as

$$\Delta \langle Q \rangle_P^{(k)} \equiv \left| \langle Q \rangle_P^{(k+1)} - \langle Q \rangle_P^{(k)} \right|, \tag{60}$$

where $\langle Q \rangle_P^{(k)}$ is the time-averaged value of the particle field $\langle Q \rangle_P$ evaluated at the end of the kth outer loop. Log–log plots of $\Delta \bar{\rho}_P$ and $\Delta \langle u^{*2} \mid x \rangle$ versus work units are shown in Figs. 15 and 16, respectively. As can be seen from comparison of these figures with Fig. 14, the particle fields converge in a similar way to the FV solutions. In other words, if the time-averaging is turned off, the changes in the particle fields remain approximately constant in the region of statistically stationary solution but they immediately start decreasing when the time-averaging is turned on.

The time-averaging parameter $\beta = 2.0$ has been used in all the results presented so far without justification. To determine the optimal value of β, log–log plots of the initial residual versus work units are displayed in Fig. 17 for $\beta = 1.5$, 2.0, 4.0, and 8.0. As can be seen in this figure, the optimal value of β that provides the best reduction in the residuals for the given computational work is about 2.0.

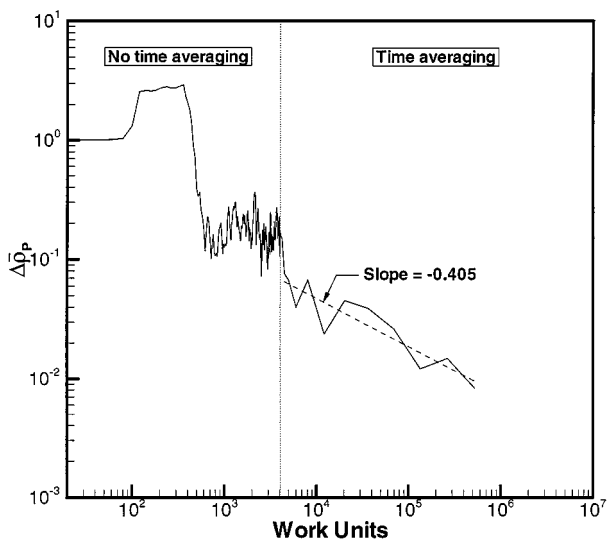

FIG. 15. Convergence history of particle density field. Time-averaging is started after 200 outer iterations with $\beta = 2.0$. The slope is calculated from linear-least-squares fit.

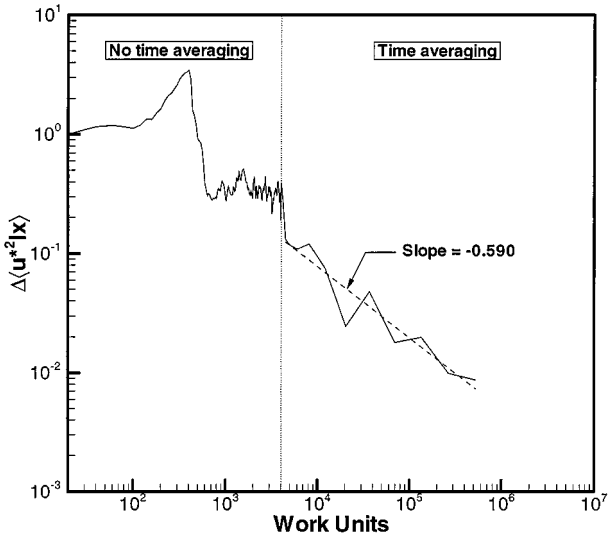

FIG. 16. Convergence history of particle field $\langle u^{*2} \mid x \rangle$. Time-averaging is started after 200 outer iterations with $\beta = 2.0$. The slope is calculated from linear-least-squares fit.

5. CONCLUSIONS

A consistent, loosely coupled, hybrid FV/particle method has been developed for the PDF equations of turbulent reactive flows. The method is designed to combine the best features and to avoid the deficiencies of the FV and particle methods. Consistency is satisfied at the level of the equations solved by the FV and particle methods. Therefore the consistency conditions are easily fulfilled. A loose coupling strategy is adopted in the hybrid method that aims at statistically stationary solutions, i.e., time-accurate solutions are excluded.

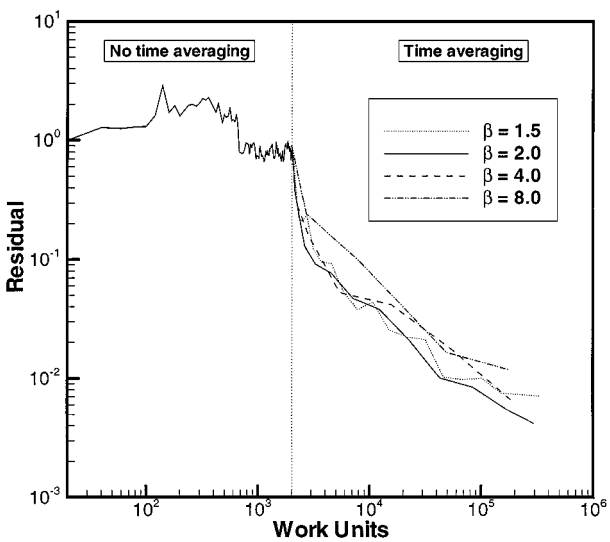

FIG. 17. Convergence histories of initial residual of FV solutions for various values of β. Time-averaging is started after 200 outer iterations.

The method has been implemented and tested in the simple setting of 1D reactive stochastic ideal flow to facilitate comprehensive numerical experiment. However, the extension of the method to higher dimensions is straightforward.

A combination of midpoint and trapezoidal rules has been employed to integrate the particle evolution equations in time and a diagonalized implicit FV algorithm has been adopted for solution of the field equations. A preconditioning method is incorporated into the FV scheme to remove the eigenvalue stiffness caused by large differences between characteristic wave speeds at low Mach numbers. A simple algorithm is also developed to eliminate the chemical stiffness induced by large source terms in the field equations. Both the FV and particle methods are found to be very robust.

The accuracy of the hybrid method has been quantified through a detailed study of numerical errors. Four types of error have been identified. Statistical error is found to scale as $(N_{pc}N_{TA})^{-1/2}$ as expected. The spatial and temporal errors scale as Δx^2 and Δt_P^2, respectively. Bias is shown not to be a dominant error in the hybrid method and scales as N_{pc}^{-1}.

A comprehensive study has been performed to demonstrate convergence of the hybrid method. The global convergence of the method has been verified. The initial residuals of the FV solutions and the changes in the particle fields evaluated at the end of successive outer iterations are found to be good measures for global convergence of mean and particle fields, respectively. The hybrid method is shown to converge at the same rate as the statistical error.

The optimal strategy for the time-averaging has also been investigated. The time-averaging is started when a statistically stationary solution is reached and doubling the total number of time steps to be taken in the particle algorithm during each successive outer cycle is demonstrated to give the best asymptotic convergence rate.

APPENDIX

The molecular weight of species α is W_α, and its gas constant is

$$R_\alpha \equiv \frac{\mathcal{R}}{W_\alpha}, \tag{61}$$

where $\mathcal{R}$ is the universal gas constant.

All energy variables are defined from the specific enthalpy of formation h_α^o at the reference temperature T_o ($T_o = 298.15$ K), and from the constant-pressure specific heat $c_{p_\alpha}(T)$ for each species. Note that thermodynamic databases are available giving the values of h_α^o and of $c_{p_\alpha}(T)$ as polynomials of T. The specific enthalpy is

$$h_\alpha(T) \equiv h_\alpha^o + \int_{T_o}^{T} c_{p_\alpha}(T')\, dT', \tag{62}$$

and the specific internal energy is

$$\epsilon_\alpha(T) \equiv h_\alpha(T) - R_\alpha T = \epsilon_\alpha^o + \int_{T_o}^{T} c_{v_\alpha}(T')\, dT', \tag{63}$$

where

$$\epsilon_\alpha^o \equiv h_\alpha^o - R_\alpha T_o, \tag{64}$$

$$c_{v_\alpha}(T) \equiv c_{p_\alpha}(T) - R_\alpha, \tag{65}$$

and the specific sensible internal energy is defined by

$$\epsilon_{s_\alpha}(T) \equiv \epsilon_\alpha(T) - \epsilon_\alpha^{so}, \tag{66}$$

where

$$\epsilon_\alpha^{so} \equiv \epsilon_\alpha^o - c_{v_\alpha}^o T_o, \tag{67}$$

with $c_{v_\alpha}^o \equiv c_{v_\alpha}(T_o)$.

For a mixture, the specific enthalpy is given by

$$h(Y, T) = \sum_\alpha Y_\alpha h_\alpha(T). \tag{68}$$

In an obvious notation, similar equations define: $\epsilon_s(\mathbf{Y}, T)$, $c_p(\mathbf{Y}, T)$, $c_v(\mathbf{Y}, T)$, and $R(\mathbf{Y}, T)$.

The conservation equations can be obtained in a number of ways. One is to differentiate Eq. (8), i.e.,

$$\begin{aligned}\frac{\partial}{\partial t}(\bar{\rho}\tilde{\phi}) &= \left\langle m^* \frac{d\phi^*}{dt}\delta(\mathbf{X}^* - \mathbf{x}) - m^*\phi^* \frac{dX_i^*}{dt}\frac{\partial}{\partial x_i}\delta(\mathbf{X}^* - \mathbf{x}) \right\rangle \\ &= \bar{\rho}\left\langle \frac{d\phi^*}{dt} \,\middle|\, \mathbf{x} \right\rangle - \frac{\partial}{\partial x_i}[\bar{\rho}\langle U_i^*\phi^* \mid \mathbf{x}\rangle].\end{aligned} \tag{69}$$

For $\phi^* = 1$, this yields the particle mean mass conservation equation

$$\frac{\partial \bar{\rho}}{\partial t} + \frac{\partial}{\partial x_i}(\bar{\rho}\tilde{U}_i) = 0. \tag{70}$$

For $\phi^* = U_j^*$, Eq. (69) and the mean of Eq. (13) yield the mean momentum equation

$$\frac{\partial}{\partial t}(\bar{\rho}\tilde{U}_j) + \frac{\partial}{\partial x_i}[\bar{\rho}\langle U_i^* U_j^* \mid \mathbf{x}\rangle] = -\frac{\partial p}{\partial x_j}. \tag{71}$$

Using the identity $U_j^* = \tilde{U}_j^* + u_j^*$, the mean momentum equation can be rewritten as

$$\frac{\partial}{\partial t}(\bar{\rho}\tilde{U}_j) + \frac{\partial}{\partial x_i}[\bar{\rho}\tilde{U}_i\tilde{U}_j + p\delta_{ij}] = -\frac{\partial}{\partial x_i}[\bar{\rho}\langle u_i^* u_j^* \mid \mathbf{x}\rangle]. \tag{72}$$

The mean energy conservation equation is obtained by substituting $\phi^* = \epsilon_s^*$ into Eq. (69)

$$\frac{\partial}{\partial t}(\bar{\rho}\tilde{\epsilon}_s) = \bar{\rho}\left\langle \frac{d\epsilon_s^*}{dt} \,\middle|\, \mathbf{x} \right\rangle - \frac{\partial}{\partial x_i}[\bar{\rho}\langle U_i^*\epsilon_s^* \mid \mathbf{x}\rangle]. \tag{73}$$

Substituting $h^* = \epsilon_s^* + p^*v^* + \sum_\alpha \epsilon_\alpha^{so} Y_\alpha^*$ into Eq. (15) and then taking the mean results in

$$\left\langle \frac{d\epsilon_s^*}{dt} \,\middle|\, \mathbf{x} \right\rangle = -p\left\langle \frac{dv^*}{dt} \,\middle|\, \mathbf{x} \right\rangle - \sum_\alpha \epsilon_\alpha^{so}\left\langle \frac{dY_\alpha^*}{dt} \right\rangle, \tag{74}$$

and the time derivative of the consistency condition $\langle m^*v^*\delta(\mathbf{X}^*[t] - \mathbf{x})\rangle = 1$ yields

$$\left\langle m^* \frac{dv^*}{dt}\delta(\mathbf{X}^*[t] - \mathbf{x}) - m^*v^* \frac{dX_i^*}{dt}\frac{\partial}{\partial x_i}\delta(\mathbf{X}^*[t] - \mathbf{x}) \right\rangle = \bar{\rho}\left\langle \frac{dv}{dt} \,\middle|\, \mathbf{x} \right\rangle - \frac{\partial \bar{U}_i}{\partial x_i} = 0. \tag{75}$$

Combining Eqs. (73), (74), and (75) gives

$$\frac{\partial}{\partial t}(\bar{\rho}\tilde{\epsilon}_s) + \frac{\partial}{\partial x_i}[\bar{\rho}\langle U_i^* \epsilon_s^* \mid \mathbf{x}\rangle] = -p\frac{\partial \bar{U}_i}{\partial x_i} + \tilde{\epsilon}_s, \tag{76}$$

where $\tilde{\epsilon}_s$ is given by Eq. (26).

From the above, we deduce the equation for

$$\tilde{e}_s \equiv \bar{\rho}\tilde{\epsilon}_s + \frac{1}{2}\bar{\rho}\tilde{U}_i\tilde{U}_i \tag{77}$$

to be

$$\begin{aligned}&\frac{\partial \tilde{e}_s}{\partial t} + \frac{\partial}{\partial x_i}[\tilde{U}_i(\tilde{e}_s + p)] \\ &\quad = \tilde{\epsilon} + p\frac{\partial}{\partial x_i}(\tilde{U}_i - \bar{U}_i) - \frac{\partial}{\partial x_i}(\bar{\rho}\langle u_i^* \epsilon_s^* \mid \mathbf{x}\rangle - \tilde{U}_j\frac{\partial}{\partial x_i}(\bar{\rho}\langle u_i^* u_j^* \mid \mathbf{x}\rangle).\end{aligned} \tag{78}$$

The evolution equation for the fluctuating particle velocity is obtained from its definition, i.e., $\mathbf{u}^* = \mathbf{U}^* - \tilde{\mathbf{U}}^*$ and from Eqs. (13), (21), and (72):

$$\begin{aligned}\frac{du_j^*}{dt} &= -\frac{1}{\rho^*}\left(\frac{\partial p}{\partial x_j}\right)^* - \frac{\partial \tilde{U}_j}{\partial t} - U_i^*\left(\frac{\partial \tilde{U}_j}{\partial x_i}\right)^* \\ &= -u_i^*\left(\frac{\partial \tilde{U}_j}{\partial x_i}\right)^* + \left(\frac{1}{\bar{\rho}^*} - \frac{1}{\rho^*}\right)\left(\frac{\partial p}{\partial x_j}\right)^* + \frac{1}{\bar{\rho}^*}\left(\frac{\partial}{\partial x_i}[\bar{\rho}\langle u_i^* u_j^* \mid \mathbf{x}\rangle]\right)^*.\end{aligned} \tag{79}$$

ACKNOWLEDGMENT

This work is supported in part by Department of Energy, Grant DE-FG02-90ER 14128.

REFERENCES

1. S. B. Pope, Computations of turbulent combustion: Progress and challenges, in *23rd International Symposium on Combustion* (The Combustion Institute, Pittsburgh, 1990), p. 591.
2. S. B. Pope, PDF methods for turbulent reactive flows, *Prog. Energy Combust. Sci.* **11**, 119 (1985).
3. S. B. Pope, Lagrangian PDF methods for turbulent flows, *Ann. Rev. Fluid Mech.* **26**, 23 (1994).
4. S. B. Pope, A Monte Carlo method for the PDF methods equations of turbulent reactive flows, *Combust. Sci. Tech.* **25**, 159 (1981).
5. W. C. Welton and S. B. Pope, PDF model calculations of compressible turbulent flows using smoothed particle hydrodynamics, *J. Comput. Phys.* **134**, 150 (1997).
6. S. V. Patankar, *Numerical Heat Transfer and Fluid Flow* (Hemisphere, Washington, DC/New York, 1980).
7. S. B. Pope and Y. L. Chen, The velocity-dissipation probability density function model for turbulent flows, *Phys. Fluids A* **2**, 1437 (1990).
8. P. R. Van Slooten, Jayesh, and S. B. Pope, Advances in PDF modeling for inhomogeneous turbulent flows, *Phys. Fluids* **10**, 246 (1998).
9. S. B. Pope, *PDF2DV*: A FORTRAN code for solving modeled joint-pdf equations in two-dimensions, unpublished, 1994.
10. S. B. Pope, *Mean Field Equations in PDF Particle Methods for Turbulent Reactive Flows*, Technical Report FDA 97-06, Cornell University, 1997.

11. B. Delarue, *Application of PDF Methods to Compressible Turbulent Reacting Flows*, Ph.D. thesis, Cornell University, 1997.
12. J. Xu and S. B. Pope, *Source of Bias in Particle-Mesh Methods for PDF Models for Turbulent Flows*, Technical Report FDA 97-01, Cornell University, 1997.
13. J. Xu and S. B. Pope, Numerical studies of PDF/Monte Carlo methods for turbulent reactive flows, *J. Comput. Phys.* **152**, 192 (1999).
14. S. M. Correa and S. B. Pope, Comparison of a Monte Carlo PDF finite-volume mean flow model with bluff-body Raman data, in *Twenty-Fourth Symp. (International) on Combust.* (The Combustion Institute, Pittsburgh, 1992), p. 279.
15. G.-C. Chang, *A Monte Carlo PDF/Finite-Volume Study of Turbulent Flames*, Ph.D. thesis, Cornell University, 1996.
16. K. Tsai and R. O. Fox, Modeling the scalar dissipation rate for a turbulent series-parallel reaction, *Chem. Eng. Sci.* **51**, 1929 (1996).
17. S. B. Pope, On the relationship between stochastic Lagrangian models of turbulence and second moment closures, *Phys. Fluids* **6 A2**, 973 (1994).
18. H. A. Wouters, P. A. Nooren, T. W. J. Peters, and D. Roekaerts, Simulation of a bluff-body stabilized diffusion flame using second moment closure and Monte Carlo methods, in *Twenty-Sixth Symp. (International) on Combust.* (The Combustion Institute, Pittsburgh, 1996), p. 177.
19. M. Nau, W. Neef, U. Maas, E. Gutheil, and J. Warnatz, Computational and experimental investigation of a turbulent non-premixed methane flame, in *Twenty-Sixth Symp. (International) on Combust.* (The Combustion Institute, Pittsburgh, 1996), p. 83.
20. F. A. Jaberi, P. J. Colucci, S. James, P. Givi, and S. B. Pope, Filtered mass density function for large eddy simulation of turbulent reacting flows, submitted.
21. M. S. Anand, S. B. Pope, and H. C. Mongia, A PDF method for turbulent recirculating flows, in *Lecture Notes in Engineering* (Springer-Verlag, New York/Berlin, 1989), p. 672.
22. D. C. Haworth and S. H. El Tahry, Probability density function approach for multidimensional turbulent flow calculations with application to in-cylinder flows in reciprocating engines, *AIAA J.* **29**, 208 (1991).
23. D. A. Caughey, Diagonal implicit multigrid algorithm for the Euler equations, *AIAA J.* **26**, 841 (1988).
24. M. Muradoglu and D. A. Caughey, *Implicit Multigrid Solution of the Preconditioned Euler Equations*, AIAA Paper 97-1951, 1997.
25. E. Turkel, A review of preconditioning methods for fluid dynamics, *Appl. Numer. Math.* **12**, 257 (1993).
26. G. Palmer, Improved flux-split algorithm applied to hypersonic flows in chemical equilibrium, *AIAA J.* **28**, 1153 (1990).
27. T. R. A. Bussing and E. M. Murman, Numerical investigation of two-dimensional H_2-Air flameholding over ramps and rearward-facing steps, *J. Propulsion* **3**, 448 (1987).
28. B. Yang and S. B. Pope, An investigation of the accuracy of manifold methods and splitting schemes in the computational implementation of combustion chemistry, *Combust. Flame* **112**, 16 (1998).
29. R. J. Kee, F. M. Rupley, and J. A. Miller, *Chemkin-II: A Fortran Chemical Kinetics Package for Analysis of Gas Phase Chemical Kinetics*, Sandia Report, SAND89-8009 B, 1993.
30. S. B. Pope, Particle method for turbulent flows: Integration of stochastic differential equations, *J. Comput. Phys.* **117**, 332 (1995).
31. R. W. Hockney and J. W. Eastwood, *Computer Simulations using Particles* (Hilger, Bristol, 1988).
32. T. D. Dreeben and S. B. Pope, *Nonparametric Estimation of Mean Fields with Application to Particle Methods for Turbulent Flows*, Technical Report FDA 92-13, Cornell University, 1992.
33. P. Kloeden and E. Platen, *Numerical Solution of Stochastic Differential Equations* (Springer-Verlag, Berlin, 1992).